Research Article | Vol. 30, No. 9 / 25 Apr 2022 / Optics Express 15060
Optics EXPRESS

# Machine learning analysis of instabilities in noise-like pulse lasers

MEHDI MABED,[1] FANCHAO MENG,[1,2] LAURI SALMELA,[3] CHRISTOPHE FINOT,[4] GOËRY GENTY,[3] AND JOHN M. DUDLEY[1,*]

[1]Institut FEMTO-ST, Université Bourgogne Franche-Comté CNRS UMR 6174, 25000 Besançon, France
[2]State Key Laboratory of Integrated Optoelectronics, College of Electronic Science and Engineering, Jilin University, Changchun 130012, China
[3]Photonics Laboratory, Tampere University, FI- 33104 Tampere, Finland
[4]Laboratoire Interdisciplinaire Carnot de Bourgogne, Université Bourgogne Franche-Comté CNRS UMR 6303, 21078 Dijon, France
[*]john.dudley@univ-fcomte.fr

**Abstract:** Neural networks have been recently shown to be highly effective in predicting time-domain properties of optical fiber instabilities based only on analyzing spectral intensity profiles. Specifically, from only spectral intensity data, a suitably trained neural network can predict temporal soliton characteristics in supercontinuum generation, as well as the presence of temporal peaks in modulation instability satisfying rogue wave criteria. Here, we extend these previous studies of machine learning prediction for single-pass fiber propagation instabilities to the more complex case of noise-like pulse dynamics in a dissipative soliton laser. Using numerical simulations of highly chaotic behaviour in a noise-like pulse laser operating around 1550 nm, we generate large ensembles of spectral and temporal data for different regimes of operation, from relatively narrowband laser spectra of 70 nm bandwidth at the -20 dB level, to broadband supercontinuum spectra spanning 200 nm at the -20 dB level and with dispersive wave and long wavelength Raman extension spanning from 1150–1700 nm. Using supervised learning techniques, a trained neural network is shown to be able to accurately correlate spectral intensity profiles with time-domain intensity peaks and to reproduce the associated temporal intensity probability distributions.



## 1. Introduction

Machine learning is an umbrella term in data science describing a range of computational and statistical techniques applied to pattern recognition, prediction, and optimization [1]. The techniques of machine learning have attracted much recent interest in ultrafast and nonlinear optics [2], where they have been applied to pulse compression and shaping [3–5], control of optical fiber laser sources [6], tailored supercontinuum generation [7,8], cluster-based classification of nonlinear structures [9], and neural network emulation of the equations of nonlinear propagation [10]. Machine learning has also been applied to the correlation of time and frequency domain features in complex instabilities associated with optical fiber propagation. In particular, although spectral intensity measurements without knowledge of spectral phase are generally considered insufficient to infer temporal information, suitably-trained neural networks have been shown to perform such predictions accurately in the case of complex spectra arising from nonlinear interactions. This has been demonstrated using modulation instability spectra to infer the intensity of localized temporal breather peaks [9], and correlating supercontinuum spectra with rogue soliton fluctuations [11]. Note that the results in Ref. [9] also analyzed experimental data based on real-time high dynamic range spectral measurements. This work has clearly shown

#455945 https://doi.org/10.1364/OE.455945
Journal © 2022 Received 9 Feb 2022; revised 24 Mar 2022; accepted 5 Apr 2022; published 20 Apr 2022

Optics EXPRESS

the tremendous potential for machine learning techniques to provide insights into a range of fluctuation phenomena in nonlinear fiber optics.

A further class of instability that has seen intense study in nonlinear optics is that associated with the operation of dissipative soliton fiber lasers [12–16]. Here, the combination of gain, loss and nonlinear Schrödinger equation (NLSE) dynamics [17,18] can lead to a wide range of behaviour including soliton explosions, soliton molecules, and chaotic intermittence [19–31]. A particularly complex "Noise-Like Pulse" (NLP) instability [32] in fiber lasers has also attracted much attention because of its observation over a wide range of laser parameter regimes, including with both normal and anomalous cavity dispersion [33], and with both narrow spectral bandwidths of 10's of nm [34–40], as well as bandwidths much greater than the gain bandwidth (100's of nm) [41–45]. A recent study of NLP operation using both real-time time lens and dispersive Fourier transform measurements and detailed numerical simulations has highlighted the central role played by soliton turbulence and supercontinuum dynamics in this regime [46].

Lasers in the NLP regime show very complex multiscale dynamics that vary from round-trip to round-trip in the cavity, and it is natural to consider whether the neural network techniques that can correlate spectral and temporal properties in single-pass propagation can also be applied to the characteristics of a NLP laser. This paper addresses this question directly. Specifically, using generalised nonlinear Schrödinger equations (GNLSE) simulations of noise-like pulse dynamics in a laser operating around 1550 nm, we generate large ensembles of spectral and temporal data for two different regimes of noise-like pulse laser operation: "narrowband" laser spectra of 70 nm bandwidth at the -20 dB level, and broadband supercontinuum spectra spanning 200 nm at the -20 dB level. Using supervised learning, a feed-forward neural network is shown to be able to accurately correlate spectral intensity profiles with time-domain intensity peaks, and to reproduce the associated temporal intensity probability distributions. In addition to further confirming the utility of machine learning in analysing nonlinear instabilities in optics, these results are of direct experimental interest. In particular, they suggest that the time-domain statistics of NLP intensity fluctuations can be inferred from applying a trained neural network to determine (predict) temporal instability characteristics from relatively straightforward real-time spectral measurements using techniques such as the dispersive Fourier transform [47] or a scanning monochromator [9].

## 2. Simulations and illustrative laser dynamics

Our numerical simulations model the laser shown in Fig. 1. This is a simplified yet typical dissipative soliton laser design that exhibits a wide range of dynamics depending on parameters such as gain, loss and filtering [15]. The cavity includes fiber of both normal and anomalous group velocity dispersion (GVD), gain in Erbium-doped fiber (EDF), a saturable absorber (SA), and a spectral filter. We simulate the laser both without and with a segment of highly nonlinear fiber (HNLF) in the cavity, allowing us to study respectively narrowband and broadband noise-like pulse dynamics.

The laser dynamics are simulated using an iterative cavity map based on a scalar GNLSE, using equivalent transfer function elements for the active medium and the saturable absorber. This approach has previously been shown to reproduce a range of single soliton and soliton molecule dynamics in agreement with experiment [29]. The model also reproduces noise-like pulse dynamics seen with a fully vectorial model [46], but with order of magnitude faster computation time which is more suitable for generating very large training data sets.

Field propagation in each fiber segment is modelled by the GNLSE written in dimensional form as follows [48]:

$$\frac{\partial A}{\partial z} + \frac{\mathrm{i}\beta_2}{2}\frac{\partial A^2}{\partial \tau^2} - \frac{\beta_3}{6}\frac{\partial A^3}{\partial \tau^3} - \frac{\hat{g}}{2} = \mathrm{i}\gamma\left(1 + \frac{\mathrm{i}}{\omega_0}\frac{\partial}{\partial \tau}\right)\left(A(z,\tau)\int_{-\infty}^{+\infty} R(t)|A(z,\tau-t)|^2 dt\right). \quad (1)$$

Optics EXPRESS

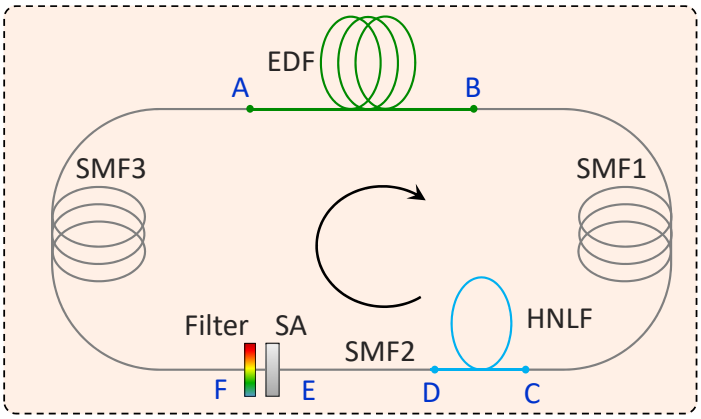


**Fig. 1.** Schematic of the NLP laser modelled here. EDF: Erbium-doped fiber. SMF: Single-mode fiber SMF28. HNLF: Highly-nonlinear fiber. SA: Saturable Absorber. Parameters for all cavity elements are given in the text.

Here, $A(z,\tau)$ is the field envelope with $z$ the propagation coordinate and $\tau$ the usual co-moving time reference frame, $\beta_2$ and $\beta_3$ are the second and third order dispersion coefficients and $\gamma$ is the nonlinear coefficient. The dispersion and nonlinearity parameters are of course different in each fiber segment (see below). The time-derivative term on the right hand side models self-steepening, and the response function $R(t) = (1-f_R)\delta(t) + f_R h_R(t)$ includes both instantaneous electronic and delayed Raman contributions. We take the Raman fraction as $f_R = 0.18$, and for $h_R$, we use the analytic approximation for silica given in Ref. [49].

The simulations used fiber lengths and parameters as follows. Segment AB consists of 10 m of Erbium-doped fiber (EDF) with normal dispersion $\beta_2 = +40\times10^{-3}\,\mathrm{ps^2\,m^{-1}}$, and nonlinear parameter $\gamma = 6.0\times10^{-3}\,\mathrm{W^{-1}\,m^{-1}}$ (based on commercial fiber OFS R37003); third-order dispersion in the EDF was neglected. Standard silica fiber segments SMF1, SMF2, and SMF3 (BC, DE, and FA) were of lengths 3 m, 4 m, and 8 m respectively, and used parameters $\beta_2 = -21.7\times10^{-3}\,\mathrm{ps^2\,m^{-1}}$, $\beta_3 = +86.0\times10^{-6}\,\mathrm{ps^3\,m^{-1}}$, and nonlinear parameter $\gamma = 1.1\times10^{-3}\,\mathrm{W^{-1}\,m^{-1}}$. When included, the supercontinuum segment CD models propagation in 2 m of HNLF with $\beta_2 = -5.23\times10^{-3}\mathrm{ps^2\,m^{-1}}$, $\beta_3 = +42.76\times10^{-6}\mathrm{ps^3\,m^{-1}}$ (zero dispersion wavelength of 1408 nm), and nonlinear parameter $\gamma = 18.4\times10^{-3}\mathrm{W^{-1}\,m^{-1}}$ (based on commercial OFS fiber). The net cavity dispersion is +0.075 $\mathrm{ps^2}$ without HNLF and +0.064 $\mathrm{ps^2}$ with the HNLF included. All dispersion and nonlinearity parameters above are specified at 1550 nm.

The gain transfer function is non-zero only in the EDF and is written in the frequency domain as: $\hat{g}(\Omega) = g_0/(1+E/E_{sat})\times1/(1+\Omega^2/\Omega_g^2)$ where $g_0$ is a small signal unsaturated gain parameter, and the frequency bandwidth $\Omega_g$ is a gain half bandwidth corresponding to 20 nm. $E = \int |A|^2 d\tau$ is the intracavity energy, and $E_{sat}$ is a gain saturation parameter [50]. $\Omega = \omega - \omega_0$ is the frequency detuning, with $\omega_0$ here corresponding to central wavelength of 1550 nm. We take parameters $g_0 = 0.73\ \mathrm{m^{-1}}$ and $E_{sat} = 3.5$ nJ in the EDF.

The saturable absorber transfer function is expressed as [51]: $T(\tau) = 1 - q_0(1 + P(\tau)/P_{sat})^{-1}$ where $q_0$ is the absorption modulation depth, $P(\tau) = |A(z,\tau)|^2$ is the instantaneous power, and $P_{sat}$ is a saturation power parameter. We use $q_0 = 0.9$ and $P_{sat} = 150$ W, consistent with previous modelling [52]. The spectral filter applied after the saturable absorber is a 10 nm intensity FWHM supergaussian function with unity transmittance at line center. A lumped linear intracavity loss of 7 dB was applied after the filter to model insertion losses and output coupling. The use of a lumped loss model is for simplicity, with the value of loss based on typical experimental values [46]. This loss includes coupling between fiber and bulk components (e.g. a nonlinear-polarization

Optics EXPRESS

rotation based saturable absorber), realistic insertion loss of the filter, as well as output coupling taps. The 10 nm bandwidth of the supergaussian filter is also based on experiment [46], with the role of the filter being to reduce the pulse bandwidth after spectral broadening before reinjection in the EDF [15]. Intrinsic fiber attenuation was neglected. Simulations with no HNLF in the cavity used $2^{13}$ points and a 120 ps time span, whereas simulations with HNLF in the cavity used $2^{17}$ points and a 650 ps time span. The numerical technique was based on an adaptive spatial step algorithm [53].

For both narrowband and broadband NLP modelling, simulations were performed to generate an ensemble of 25,000 pairs of spectral and temporal intensity profiles at point D in the cavity. These data were extracted from an extended simulation run after removing the initial evolution phase (typically ~ 1000 roundtrips). This approach captures the shot-to-shot fluctuations associated with the NLP regime of operation. Of the 25,000 sets of simulation data, 15,000 were used in the training the neural network described below, and 10,000 used for subsequent testing.

Illustrative simulation results for the narrowband and broadband cases are shown in Fig. 2 and Fig. 3 respectively. In each figure, we first illustrate the expected NLP dynamics by plotting the simulated (a) spectral and (b) temporal evolution over one cavity trip. The narrowband dynamics in Fig. 2(a,b) illustrate typical evolution in this regime with initial incoherent spectral broadening in the EDF associated with the generation of random temporal pulses with positive chirp. These pulses subsequently undergo temporal compression in the segments SMF1 and SMF2 before significant changes in both spectral and temporal characteristics are seen in segment SMF3 as a result of the action of the saturable absorber and spectral filter. The broadband dynamics in Fig. 3(a,b) show similar incoherent evolution but in addition show the large supercontinuum broadening in the HNLF segment which includes dispersive wave generation around 1150 nm and long wavelength edge extension above 1700 nm.

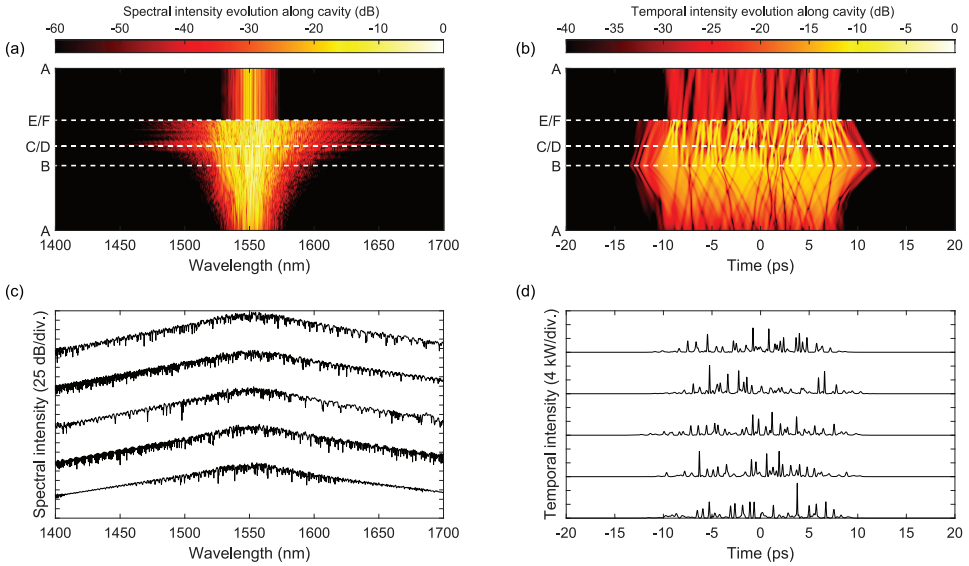


**Fig. 2.** Numerical simulations in the narrowband NLP regime with no HNLF in the cavity. (a) and (b) show respectively the spectral and temporal evolution over one roundtrip in the cavity. (c) and (d) illustrate the shot-to-shot fluctuations by plotting 5 spectral and temporal intensity profiles (after the SMF1 segment) associated with 5 consecutive roundtrips.

The results in Fig. 2(c) and Fig. 3(c) show a selection of 5 spectra from the ensemble, with the black lines in Fig. 2(d) and Fig. 3(d) showing the corresponding temporal intensity. The extracted intracavity profiles in Fig. 2 are taken at point C at the output of SMF1 while those

Optics EXPRESS

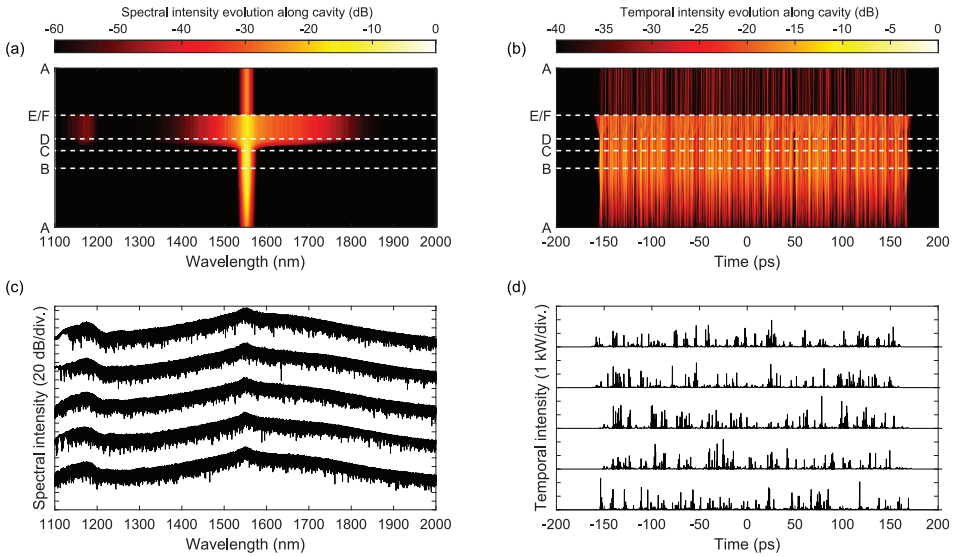


**Fig. 3.** Numerical simulations in the broadband NLP regime with HNLF in the cavity. (a) and (b) show respectively the spectral and temporal evolution over one roundtrip in the cavity. (c) and (d) illustrate the shot-to-shot fluctuations by plotting 5 spectral and temporal intensity profiles (after the HNLF segment) associated with 5 different (consecutive) roundtrips. Note the different time and wavelength spans in this figure compared to Fig. 2.

in Fig. 3 are taken at point D corresponding to the output of the HNLF. Experimentally these profiles would be measured using low transmission output couplers at these points, but these are not included in our model. As seen in the evolution plots, both these points show typical complex NLP structure. We clearly see how the NLP laser dynamics lead to large shot-to-shot variations between different results in the ensemble, and the results also illustrate the qualitative differences between the narrowband and broadband NLP regimes. Note that these temporal and spectral variations are also associated with fluctuations in energy between different roundtrips which are typically ~5 %, with similar mean intracavity energies for the narrowband (13.4 nJ at point C) and the broadband (12.3 nJ at point D) cases.

Note however that although the two regimes of operation have comparable energies, the spectral and temporal properties are very different. Specifically, for the narrowband case, we see an approximately symmetric spectrum of 70 nm -20 dB bandwidth and a ~ 15 ps pulse envelope containing approximately 50 temporal peaks of median peak power and duration 1 kW and 0.15 ps respectively. In contrast for the broadband case, the spectrum is highly asymmetric with 200 nm -20 dB bandwidth, and the corresponding temporal characteristics are associated with a ~ 300 ps pulse envelope containing approximately 300 temporal peaks of median peak power and duration 0.2 kW and 0.05 ps respectively. Note that although the -20 dB bandwidth in the broadband case is 200 nm, the full wavelength span from the generated dispersive wave to the long wavelength Raman extension spans from 1150–1700 nm. Significantly, although the NLP dynamics are very different from the single-pass propagation cases studied previously [9,11], we shall see in the next section that a suitably trained neural network is still able to predict the peak temporal intensity of the pulses under the envelope based on only the spectral data, with this approach being particularly robust for the narrowband case.

Optics EXPRESS

## 3. Neural network training and validation

Our objective is to apply machine learning to extract temporal properties of the NLP laser field from only spectral data. As with studies of modulation instability, we focus on predicting the peak temporal intensity, as it is this that is of interest for analysing effects such as the appearance of long tails in probability distributions of shot-to-shot fluctuations [9]. To this end, we used a supervised feed-forward neural network to correlate the full NLP spectrum and the peak power of the highest intensity peak from amongst the many temporal peaks in the NLP field.

A schematic of the neural network is shown in Fig. 4. The network input is a single-shot spectral intensity vector $X^{(0)} = [x_1^{(0)}, x_2^{(0)}, \ldots, x_{N_0}^{(0)}]$ of length $N_0$, whilst the network output is a scalar equal to the maximum intensity of the corresponding NLP temporal profile (detected using a standard peak search algorithm). Before being fed into the input layer, the high-resolution simulated NLP spectra ($2^{13}$ and $2^{17}$ points for the narrowband and broadband cases respectively) are converted to logarithmic scale in dB and preprocessed by sampling between [1350 1850] nm (narrowband) and [1100 3200] nm (broadband), and then convolving with a 1.1 nm FWHM Gaussian, and binning into 1 nm wide bins. This process replicates potential experimental measurements [9], and yields input vectors of length 500 and 2100 points for the narrowband and broadband data respectively. The network uses two fully-connected hidden layers of 100 and 30 neurons (narrowband) and 300 and 100 neurons (broadband), and the output of each network node is calculated as a linear combination of the outputs from the neurons in the previous layer. The weighted sum is then passed through a hyperbolic tangent nonlinear activation function for each neuron. For both narrowband and broadband cases, the network (coded in MATLAB) is trained from an ensemble of 15,000 simulations using a standard stochastic gradient descent technique, training the network over 150 epochs with a fixed learning rate of 0.01 and no momentum or dropout techniques. The network optimisation uses a mean squared error (L2-norm) cost function calculated from the network output and the target training data. This is a standard approach [54], and has been previously described in Refs [9,11]. After the training phase, the network was tested using an independent set of 10,000 simulations that were not used in training. The sizes of the training and testing data sets were chosen heuristically based on results from previous studies of single-pass propagation [9,11].

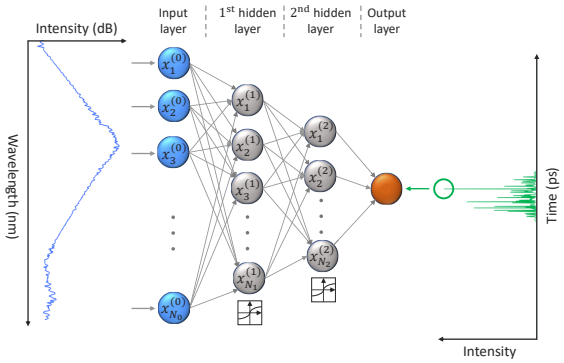


**Fig. 4.** Schematic of the feed-forward neural network used in this work. (a) The input is a single-shot spectral intensity vector $X^{(0)} = [x_1^{(0)}, x_2^{(0)}, \ldots, x_{N_0}^{(0)}]$ of length $N_0$ corresponding to the sampled and convolved spectral data from simulations. The 2 hidden layers have respectively 100 and 30 neurons (narrowband case) and 300 and 100 neurons (broadband case).

We first consider results for the narrowband case, shown in Fig. 5 where we plot the peak powers of the highest intensity temporal peak predicted by the network based on the single-shot

Optics EXPRESS

spectra input, and the expected ("ground truth") values extracted from the known simulated time-domain profiles. For visualization, we use a false colour representation (with a logarithmic scale) where predictions are grouped into bins of constant area, and a histogram plots the density of data points in each bin. We convert the histogram into normalised form (similar to a probability density) such that the integral over the expected and predicted axes is unity (leading to the dimensions of $kW^{-2}$ for the plotted point densities.

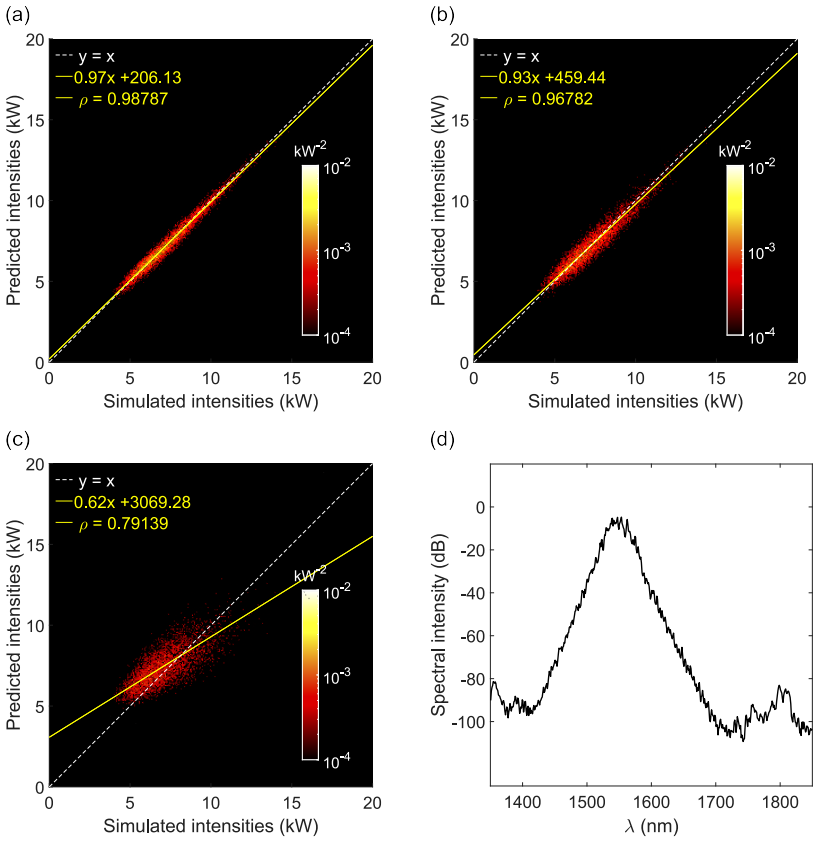


**Fig. 5.** Results for the narrowband regime of operation showing neural network prediction of the highest intensity temporal peak based only on input spectral data for an ensemble of 10,000 simulations not used in the training phase. We compare the predicted peak power of the highest intensity temporal peak with the known result from simulations for input spectra: (a) with the full dynamic range of simulations, (b) truncated to a dynamic range of 50 dB, (c) truncated to a dynamic range of 30 dB. For all sub-figures, the logarithmic histograms are shown using a false colour representation plotting the normalized density of points grouped into bins of constant area. The bin resolution is 70 W. The dashed white line shows the 1-to-1 correspondence and the yellow line is a linear fit along with the correlation coefficient $\rho$. (d) shows a typical single shot spectrum used as input to the network (over its full dynamic range.)

In the context of linking this approach with experiment, Fig. 5(a) shows results for the data with the full dynamic range of the simulations, and Fig. 5(b) and (c) show results at reduced dynamic range with truncation of the spectra at the network input to dynamic ranges of 50 dB and 30 dB respectively. Since we are trying to replicate how experiments may be carried out with such data, we keep the spectral resolution constant as we reduce the dynamic range so the number

Optics EXPRESS

of data points processed by the network decreases for lower dynamic range corresponding to 150 and 85 points for dynamic ranges of 50 dB and 30 dB respectively. Note that we tested the effect of dynamic range reduction on the network performance in two ways: (i) by completely deactivating the neurons in the network at spectral values below the specified dynamic range limit; and (ii) by adding an artificial spectral floor (either constant or with noise) at the dynamic range limit. Both approaches yielded essentially indistinguishable results. The results we present here correspond to neuron deactivation. For completeness, Fig. 5(d) shows a typical single-shot spectrum from the simulated data used as input to the network, plotted over its full dynamic range.

The results in Fig. 5(a) using input spectra with the full dynamic range of the simulations correspond to identical training and testing conditions. We see here very strong clustering around the ideal $x = y$ relation (white dashed line), and a Pearson correlation coefficient of $\rho = 0.99$ associated with a linear fit to the predicted data (solid yellow line). Importantly, we find that the predictions made using this network are still very good even if we truncate the input spectra to have a reduced dynamic range such that the training and test data are not strictly the same.

Typical results are shown in Fig. 5(b) and Fig. 5(c) for dynamic ranges of 50 dB and 30 dB respectively, where we see that 50 dB truncation yields excellent correlation ($\rho = 0.97$) although at the more severe truncation at 30 dB, we obtain poorer correlation ($\rho = 0.79$) and we see a clear bias between the expected linear relation (dashed white line) and the linear fit to predictions (yellow line). These results are consistent with similar previous studies of modulation instability with similar spectral characteristics [9], where accurate spectral-based temporal intensity prediction was reported for 60 dB dynamic range whilst prediction failed at 25 dB dynamic range.

A more stringent test of the predictive capability of the neural network is to assess its performance for the more complex broadband NLP regime when higher-order dynamics such as the Raman effect can play an important role. These results are shown in Fig. 6. Here, the shot-to-shot spectra are highly asymmetric and they also extend over a broader bandwidth, and the corresponding temporal properties are also significantly more complex than in the narrowband case. This additional complexity is reflected in the poorer performance of the neural network in this case. The results in Fig. 6(a) correspond to input spectra with the full dynamic range of the simulations, and although the Pearson correlation coefficient of $\rho = 0.92$ is high, these results are clearly inferior to those shown in Fig. 5(a) for the narrowband case. Note here that the clearer visual pixellation in the density plots in Fig. 6. arise from the reduced span of peak powers when compared to the results in Fig. 5. The bin resolutions used for the histogram plots are 70 W in both Figs. 5 and 6.

The results with reduced dynamic range in Fig. 6(b) and Fig. 6(c) correspond to 80 dB and 50 dB truncation respectively. Fig. 6(d) shows a typical single-shot spectrum used as input to the network plotted over its full dynamic range. As explained above, the number of data points processed by the network decreases for lower dynamic range and corresponds to 1380 and 650 points for dynamic ranges of 80 dB and 50 dB respectively. These plots clearly show that a dynamic range of 50 dB which yielded good results for the narrowband case yields poor results for the broadband case. Note that additional tests by training over a larger set or exploring a larger range of hyperparameters did not yield improved results for reduced dynamic range, suggesting that the degree of complexity inherent to the broadband NLP pulses requires over 80 dB dynamic range for acceptable performance. Figure 7 summarises results showing how the correlation coefficient varies with dynamic range truncation for the two cases. The results above suggest input spectral dynamics ranges of 50 dB for the narrowband regime and 80 dB for the broadband regime yield acceptable predictions with correlation coefficients exceeding 0.9. For these cases, we have also confirmed that the probability distributions for the peak temporal intensities of the NLP pulses reconstructed from the neural network predictions are in good

Optics EXPRESS

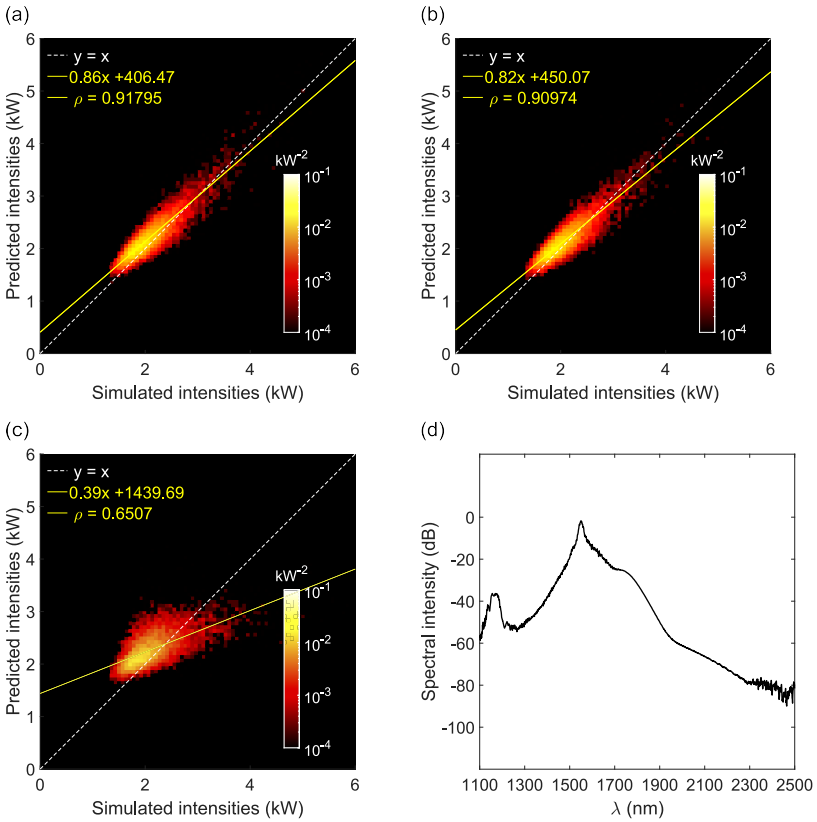


**Fig. 6.** Results for the broadband regime of operation showing neural network prediction of the highest intensity temporal peak based only on input spectral data for an ensemble of 10,000 simulations not used in the training phase. We compare the predicted peak power of the highest intensity temporal peak with the known result from simulations for input spectra: (a) with the full dynamic range of simulations, (b) truncated to a dynamic range of 80 dB, (c) truncated to a dynamic range of 50 dB. For all sub-figures, the logarithmic histograms are shown with a false colour representation plotting the normalized density of points grouped into bins of constant area. The bin resolution is 70 W. The dashed white line shows the 1-to-1 correspondence and the yellow line is a linear fit along with the correlation coefficient $\rho$. (d) shows a typical single shot spectrum used as input to the network (over its full dynamic range.)

Optics EXPRESS

agreement with those from the direct numerical simulations. These results are shown in Fig. 8(a) for the narrowband regime and Fig. 8(b) for the broadband regime, and we plot in both cases the normalised probability distributions for the intensities of the highest temporal peaks computed directly from the GNLSE simulations (blue line) compared with the probability distributions computed from the neural network predictions (red dashed line). We note in particular the very good agreement in the distribution tails in both cases, spanning over two orders of magnitude.

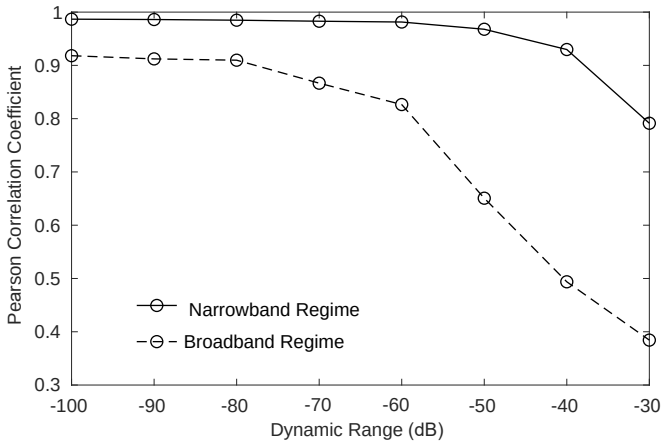


**Fig. 7.** Summarising the achieved performance of the neural network in predicting intensities of the highest temporal peaks for spectra truncated at different dynamic ranges. The results for the narrowband case (solid line and markers) are clearly superior than for the broadband case (dashed line and markers).

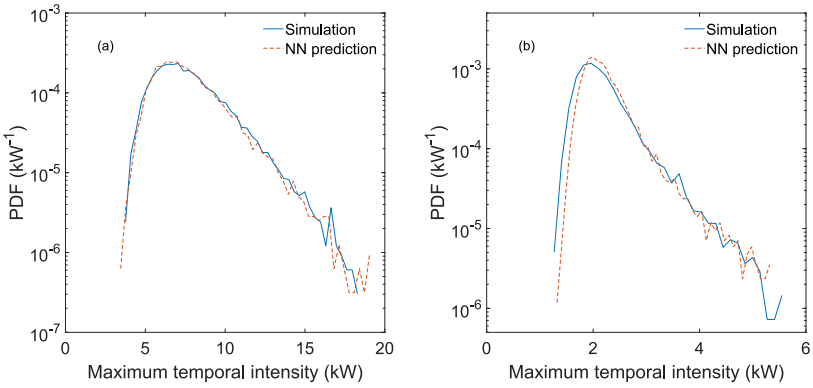


**Fig. 8.** Probability distributions for the highest intensity temporal peaks based only on input spectral data reconstructed from the neural network (NN) predictions (red dashed lines) compared with those from the direct numerical simulations (blue lines). (a) shows results for the narrowband regime with NN inputs truncated to a dynamic range of 50 dB (b) for the broadband regime with NN inputs truncated to a dynamic range of 80 dB.

A further point to note here is that all results shown above were obtained using the same initial data convolution and binning bandwidth of 1 nm. Additional simulations show that there is a decrease in network accuracy as this bandwidth is increased, but that acceptable correlation coefficients of 0.9 can still be obtained with bandwidths up to ~10 nm for both narrowband and

Optics EXPRESS

broadband cases. It is also natural to ask whether a neural network can also correlate spectral and temporal properties over a broader range of pulse energies, through variation of the saturation energy $E_{sat}$. In this regard, we first note that decreasing $E_{sat}$ to lower values approaching ~1 nJ leads to the laser entering different regimes of single pulse and/or molecule states that can exhibit either stable dynamics or various forms of instability [30,46]. In fact, neural networks have been used to correlate the spectral and temporal properties of such states [55], but this is a very different mode of operation than the NLP regime which we study here. In the context of the NLP instabilities, we have also tested the approach described in this paper for higher values of $E_{sat}$ up to ~10 nJ, and the neural network was successfully trained to yield results comparable to those above. Performing simulations to generate large training data sets at even larger values of $E_{sat}$ is computationally expensive, but we would fully expect this approach to work for all values of $E_{sat}$ where the same general NLP dynamics and similar temporal and spectral structures were observed.

## 4. Discussion and conclusions

The results in this paper using a neural network to analyse noise-like pulse laser instabilities represent a further extension of the use of machine learning techniques in analysing nonlinear dynamics [2,5,9–11]. In particular, the instabilities that we have studied here in a noise-like pulse fiber laser are of a different multiscale nature than those seen in single-pass fiber propagation, and yet a suitably-trained neural network is still successful in predicting temporal properties from only spectral intensity data.

These results provide a further example of the potential of machine learning to complement current experimental techniques by allowing the temporal characteristics of ultrashort localized structures to be determined from only spectral intensity measurements. However, our results also highlight the importance of being able to perform spectral measurements with a dynamic range sufficient to fully capture the desired temporal properties after analysis by the network. The results of our quantitative study show that acceptable predictive results (correlation exceeding 0.9) are obtained with 50 dB dynamic range with narrowband pulses, and 80 dB dynamic range with broadband pulses. Such high dynamic ranges, even for real time measurements, are feasible using adapted monochromator-based approaches. Finally, we note that it may also be possible to consider improvements to this approach using different network architectures including e.g. convolutional layers.

**Funding.** Academy of Finland (318082, 320165 Flagship PREIN, 333949); Centre National de la Recherche Scientifique (MITI Evènements Rares 2022); Agence Nationale de la Recherche (ANR-15-IDEX-0003, ANR-17-EURE-0002, ANR-20-CE30-0004).

**Disclosures.** The authors declare no conflicts of interest.

**Data availability.** Data underlying the results presented in this paper are available from the authors upon reasonable request.

## References

1. M. I. Jordan and T. M. Mitchell, "Machine learning: Trends, perspectives, and prospects," Science **349**(6245), 255–260 (2015).
2. G. Genty, L. Salmela, J. M. Dudley, D. Brunner, A. Kokhanovskiy, S. Kobtsev, and S. K. Turitsyn, "Machine learning and applications in ultrafast photonics," Nat. Photonics **15**(2), 91–101 (2021).
3. C. A. Farfan, J. Epstein, and D. B. Turner, "Femtosecond pulse compression using a neural-network algorithm," Opt. Lett. **43**(20), 5166–5169 (2018).
4. S. Boscolo and C. Finot, "Artificial neural networks for nonlinear pulse shaping in optical fibers," Opt. Laser Technol. **131**, 106439 (2020).
5. S. Boscolo, J. M. Dudley, and C. Finot, "Modelling self-similar parabolic pulses in optical fibres with a neural network," Results in Opt. **3**, 100066 (2021).
6. F. Meng and J. M. Dudley, "Toward a self-driving ultrafast fiber laser," Light: Sci. Appl. **9**(1), 26 (2020).

Optics EXPRESS


7. B. Wetzel, M. Kues, P. Roztocki, C. Reimer, P.-L. Godin, M. Rowley, B. E. Little, S. T. Chu, E. A. Viktorov, D. J. Moss, A. Pasquazi, M. Peccianti, and R. Morandotti, "Customizing supercontinuum generation via on-chip adaptive temporal pulse-splitting," Nat. Commun. **9**(1), 4884 (2018).
8. L. Michaeli and A. Bahabad, "Genetic algorithm driven spectral shaping of supercontinuum radiation in a photonic crystal fiber," J. Opt. **20**(5), 055501 (2018).
9. M. Närhi, L. Salmela, J. Toivonen, C. Billet, J. M. Dudley, and G. Genty, "Machine learning analysis of extreme events in optical fibre modulation instability," Nat. Commun. **9**(1), 4923 (2018).
10. L. Salmela, N. Tsipinakis, A. Foi, C. Billet, J. M. Dudley, and G. Genty, "Predicting ultrafast nonlinear dynamics in fibre optics with a recurrent neural network," Nat. Mach. Intell. **3**(4), 344–354 (2021).
11. L. Salmela, C. Lapre, J. M. Dudley, and G. Genty, "Machine learning analysis of rogue solitons in supercontinuum generation," Sci. Rep. **10**(1), 9596 (2020).
12. N. Akhmediev and A. Ankiewicz, eds., *Dissipative Solitons* (Springer, 2005).
13. P. Grelu and N. Akhmediev, "Dissipative solitons for mode-locked lasers," Nat. Photonics **6**(2), 84–92 (2012).
14. S. K. Turitsyn, N. N. Rozanov, I. A. Yarutkina, A. E. Bednyakova, S. Fedorov, O. V. Shtyrina, and M. P. Fedoruk, "Dissipative solitons in fiber lasers," Phys.-Usp. **59**(7), 642–668 (2016).
15. R. I. Woodward, "Dispersion engineering of mode-locked fibre lasers," J. Opt. **20**(3), 033002 (2018).
16. W. Fu, L. G. Wright, P. Sidorenko, S. Backus, and F. W. Wise, "Several new directions for ultrafast fiber lasers [Invited]," Opt. Express **26**(8), 9432 (2018).
17. K. J. Blow and N. J. Doran, "Global and local chaos in the pumped nonlinear Schrödinger equation," Phys. Rev. Lett. **52**(7), 526–529 (1984).
18. B. M. Herbst and M. J. Ablowitz, "Numerically induced chaos in the nonlinear schrödinger equation," Phys. Rev. Lett. **62**(18), 2065–2068 (1989).
19. A. F. J. Runge, C. Aguergaray, N. G. R. Broderick, and M. Erkintalo, "Coherence and shot-to-shot spectral fluctuations in noise-like ultrafast fiber lasers," Opt. Lett. **38**(21), 4327 (2013).
20. D. V. Churkin, S. Sugavanam, N. Tarasov, S. Khorev, S. V. Smirnov, S. M. Kobtsev, and S. K. Turitsyn, "Stochasticity, periodicity and localized light structures in partially mode-locked fibre lasers," Nat. Commun. **6**(1), 7004 (2015).
21. Y.-Q. Huang, Y.-L. Qi, Z.-C. Luo, A.-P. Luo, and W.-C. Xu, "Versatile patterns of multiple rectangular noise-like pulses in a fiber laser," Opt. Express **24**(7), 7356–7363 (2016).
22. K. Krupa, K. Nithyanandan, U. Andral, P. Tchofo-Dinda, and P. Grelu, "Real-Time Observation of Internal Motion within Ultrafast Dissipative Optical Soliton Molecules," Phys. Rev. Lett. **118**(24), 243901 (2017).
23. G. Herink, F. Kurtz, B. Jalali, D. R. Solli, and C. Ropers, "Real-time spectral interferometry probes the internal dynamics of femtosecond soliton molecules," Science **356**(6333), 50–54 (2017).
24. X. Liu, X. Yao, and Y. Cui, "Real-time observation of the buildup of soliton molecules," Phys. Rev. Lett. **121**(2), 023905 (2018).
25. P. Ryczkowski, M. Närhi, C. Billet, J. M. Merolla, G. Genty, and J. M. Dudley, "Real-time full-field characterization of transient dissipative soliton dynamics in a mode-locked laser," Nat. Photonics **12**(4), 221–227 (2018).
26. A. Klein, G. Masri, H. Duadi, K. Sulimany, O. Lib, H. Steinberg, S. A. Kolpakov, and M. Fridman, "Ultrafast rogue wave patterns in fiber lasers," Optica **5**(7), 774–778 (2018).
27. J. Peng, M. Sorokina, S. Sugavanam, N. Tarasov, D. V. Churkin, S. K. Turitsyn, and H. Zeng, "Real-time observation of dissipative soliton formation in nonlinear polarization rotation mode-locked fibre lasers," Commun. Phys. **1**(1), 20 (2018).
28. X. Liu and Y. Cui, "Revealing the behavior of soliton buildup in a mode-locked laser," Adv. Photonics **1**(1), 1–14 (2019).
29. C. Lapre, C. Billet, F. Meng, P. Ryczkowski, T. Sylvestre, C. Finot, G. Genty, and J. M. Dudley, "Real-time characterization of spectral instabilities in a mode-locked fibre laser exhibiting soliton-similariton dynamics," Sci. Rep. **9**(1), 13950 (2019).
30. F. Meng, C. Lapre, C. Billet, G. Genty, and J. M. Dudley, "Instabilities in a dissipative soliton-similariton laser using a scalar iterative map," Opt. Lett. **45**(5), 1232–1235 (2020).
31. R. Zhou, X. Liu, D. Yu, Q. Li, and H. Y. Fu, "Versatile multi-soliton patterns of noise-like pulses in a passively mode-locked fiber laser," Opt. Express **28**(2), 912–923 (2020).
32. M. Horowitz, Y. Barad, and Y. Silberberg, "Noiselike pulses with a broadband spectrum generated from an erbium-doped fiber laser," Opt. Lett. **22**(11), 799–801 (1997).
33. Y. Jeong, L. A. Vazquez-Zuniga, S. Lee, and Y. Kwon, "On the formation of noise-like pulses in fiber ring cavity configurations," Opt. Fiber Technol. **20**(6), 575–592 (2014).
34. D. Y. Tang, L. M. Zhao, and B. Zhao, "Soliton collapse and bunched noise-like pulse generation in a passively mode-locked fiber ring laser," Opt. Express **13**(7), 2289–2294 (2005).
35. S. Kobtsev, S. Kukarin, S. Smirnov, S. Turitsyn, and A. Latkin, "Generation of double-scale femto/pico-second optical lumps in mode-locked fiber lasers," Opt. Express **17**(23), 20707–20713 (2009).
36. O. Pottiez, R. Grajales-Couti no, B. Ibarra-Escamilla, E. Kuzin, and J. Hernández-García, "Adjustable noiselike pulses from a figure-eight fiber laser," Appl. Opt. **50**(25), E24–E31 (2011).
37. C. Lecaplain and P. Grelu, "Rogue waves among noiselike-pulse laser emission: An experimental investigation," Phys. Rev. A **90**(1), 013805 (2014).

Optics EXPRESS


38. B. Li, J. Kang, S. Wang, Y. Yu, P. Feng, and K. K. Y. Wong, "Unveiling femtosecond rogue-wave structures in noise-like pulses by a stable and synchronized time magnifier," Opt. Lett. **44**(17), 4351–4354 (2019).
39. Z. Wang, K. Nithyanandan, A. Coillet, P. Tchofo-Dinda, and P. Grelu, "Buildup of incoherent dissipative solitons in ultrafast fiber lasers," Phys. Rev. Res. **2**(1), 013101 (2020).
40. Y. Du, S. V. Sergeyev, Z. Xu, M. Han, X. Shu, and S. K. Turitsyn, "Alternation of the mode synchronization and desynchronization in ultrafast fiber laser," Laser Photonics Rev. **14**, 1900219 (2020).
41. L. A. Vazquez-Zuniga and Y. Jeong, "Super-broadband noise-like pulse erbium-doped fiber ring laser with a highly nonlinear fiber for raman gain enhancement," IEEE Photonics Technol. Lett. **24**(17), 1549–1551 (2012).
42. T. North and M. Rochette, "Raman-induced noiselike pulses in a highly nonlinear and dispersive all-fiber ring laser," Opt. Lett. **38**(6), 890–892 (2013).
43. H. Santiago-Hernandez, O. Pottiez, R. Paez-Aguirre, H. E. Ibarra-Villalon, A. Tenorio-Torres, M. Duran-Sanchez, B. Ibarra-Escamilla, E. A. Kuzin, and J. C. Hernandez-Garcia, "Generation and characterization of erbium-Raman noise-like pulses from a figure-eight fibre laser," Laser Phys. **25**(4), 045106 (2015).
44. X. Wang, A. Komarov, M. Klimczak, L. Su, D. Tang, D. Shen, L. Li, and L. Zhao, "Generation of noise-like pulses with 203 nm 3-dB bandwidth," Opt. Express **27**(17), 24147–24153 (2019).
45. X. Li, S. Zhang, J. Liu, D. Yan, C. Wang, and Z. Yang, "Symbiotic coexistence of noise-like pulses," Opt. Express **29**(19), 30449–30460 (2021).
46. F. Meng, C. Lapre, C. Billet, T. Sylvestre, J.-M. Merolla, C. Finot, S. K. Turitysn, G. Genty, and J. M. Dudley, "Intracavity incoherent supercontinuum dynamics and rogue waves in a broadband dissipative soliton laser," Nat. Commun. **12**(1), 5567 (2021).
47. D. R. Solli, C. Ropers, P. Koonath, and B. Jalali, "Optical rogue waves," Nature **450**(7172), 1054–1057 (2007).
48. J. M. Dudley, G. Genty, and S. Coen, "Supercontinuum generation in photonic crystal fiber," Rev. Mod. Phys. **78**(4), 1135–1184 (2006).
49. G. P. Agrawal, *Nonlinear Fiber Optics* (Academic, 2013).
50. I. A. Yarutkina, O. V. Shtyrina, M. P. Fedoruk, and S. K. Turitsyn, "Numerical modeling of fiber lasers with long and ultra-long ring cavity," Opt. Express **21**(10), 12942 (2013).
51. B. Oktem, C. Ülgüdür, and F. Ömer Ilday, "Soliton–similariton fibre laser," Nat. Photonics **4**(5), 307–311 (2010).
52. W. H. Renninger, A. Chong, and F. W. Wise, "Pulse shaping and evolution in normal-dispersion mode-locked fiber lasers," IEEE J. Sel. Top. Quantum Electron. **18**(1), 389–398 (2012).
53. J. M. Dudley and J. R. Taylor, *Supercontinuum Generation in Optical Fiber* (Cambridge University, 2010).
54. M. Nielsen, *Neural Networks and Deep Learning* (Determination, 2015).
55. C. Li, J. He, R. He, Y. Liu, Y. Yue, W. Liu, L. Zhang, L. Zhu, M. Zhou, K. Zhu, and Z. Wang, "Analysis of real-time spectral interference using a deep neural network to reconstruct multi-soliton dynamics in mode-locked lasers," APL Photonics **5**(11), 116101 (2020).